

Multiphysics Modeling of Surface Diffusion Coupled with Large Deformation in 3D Solids

Jaemin Kim^{a,*}, Keon Ho Kim^a, Nikolaos Bouklas^b

^aThe Oden Institute for Computational Engineering and Sciences, The University of Texas at Austin, Austin, TX 78712, USA

^bSibley School of Mechanical and Aerospace Engineering, Cornell University, Ithaca, NY 14853, USA

Abstract

We present a comprehensive theoretical and computational model that explores the behavior of a thin hydrated film bonded to a non-hydrated / impermeable soft substrate in the context of surface and bulk elasticity coupled with surface diffusion kinetics. This type of coupling can manifest as an integral aspect in diverse engineering processes encountered in optical interference coatings, tissue engineering, soft electronics, and can prove important in design process for the next generation of sensors and actuators, especially as the focus is shifted to systems in smaller lengthscales. The intricate interplay between solvent diffusion and deformation of the film is governed by surface poroelasticity, and the viscoelastic deformation of the substrate. While existing methodologies offer tools for studying coupled poroelasticity involving solvent diffusion and network deformation, there exists a gap in understanding how coupled poroelastic processes occurring in a film attached to the boundary of a highly deformable solid can influence its response. In this study, we introduce a non-equilibrium thermodynamics formulation encompassing the multi-physical processes of surface poroelasticity and bulk viscoelasticity, complemented by a corresponding finite element implementation. Our approach captures the complex dynamics between the finite deformation of the substrate and solvent diffusion on the surface. This work contributes valuable insights, particularly in scenarios where the coupling of surface diffusion kinetics and substrate elasticity is an important design factor.

Keywords: Soft materials, Hydrogels, Surface diffusion, Viscoelasticity, Non-equilibrium

1. Introduction

The field of soft solid mechanics has attracted significant attention due to its diverse range of potential applications, spanning from the design of biocompatible materials (Lin et al., 2016; Yang et al., 2020) to investigations in mechanobiology (Baker et al., 2015; Hall et al., 2016; Kim et al., 2020, 2023a) and tissue engineering (Mailand et al., 2022; Rossy et al., 2023). Additionally, it extends to advancements in soft robotics (Martinez et al., 2014; Wallin et al., 2018), soft electronics (Hu et al., 2023; Fu et al., 2023), microfluidic device fabrication (Cheng et al., 2007; Kopecek, 2009), and the development of drug delivery systems (Park et al., 2017; Chen et al., 2020). In these applications, the hydrogels and porous polymeric films are often used for coating the substrate (Wiener et al., 2014; Delavoipière et al., 2018; Moreau et al., 2016; Huo et al., 2022), and the interaction of films with soft substrates is pivotal. Here, the deformation of these substrate materials plays a fundamental role in determining the dynamic response of coated soft solids (Lucantonio et al., 2016; Song et al., 2020, 2023). For instance, surface instabilities (Hui et al., 2021) arise due to confinement during swelling or externally applied compressive stresses (Bouklas and Huang, 2012; Bouklas et al., 2015). A similar thin-film/substrate setup is also widely adopted in the study of mechanobiology, where cell migration and formation of epithelial sheets can occur on soft solid substrates (Reinhart-King et al., 2005; Tse and Engler, 2010; Rens and Merks, 2020). Therefore, understanding the transient responses of multiphysical surface processes occurring on highly-deforming soft solid substrates is imperative for ensuring improved predictive capabilities for these diverse

*Corresponding Author

Email address: jaemin.kim@austin.utexas.edu (Jaemin Kim)

applications (Xu et al., 2020; Björklund et al., 2023). In continuum thermodynamics, the non-equilibrium processes are often modeled with internal variables, capturing time-dependent mechanical behaviors, such as relaxation and diffusion (Holzapfel, 2000; Song et al., 2023).

Motivated by applications in diverse and emerging fields, we investigate a hydrogel film experiencing solvent diffusion during the deformation of a three-dimensional (3D) soft but impermeable substrate to which it is rigidly bonded. Building upon prior works (Steinmann, 2008; Javili and Steinmann, 2009, 2010; McBride et al., 2011; Lucantonio et al., 2016; Kim et al., 2023b), we model the film in the context of surface poroelasticity. As the substrate is deformed the solvent concentration in the film can change depending on the location on the surface and deformation history at that point. In our prior research (Kim et al., 2023b), we established a set of governing equations for surface poroelasticity, specifically modeling the coupled transport of solvent and the elasticity of the polymer network on the film. Notably, considering that the film is tethered to the substrate surface, we describe it as a two-dimensional (2D) structure. This work is also relevant to cases where an impermeable polymer body has a functionalized hydrophilic surface, enabling surface diffusion upon deformation of the bulk, and surface elasticity also becomes important as one moves to smaller lengthscales. While earlier studies laid the theoretical groundwork, finite element implementation that considers surface poroelasticity and bulk viscoelasticity (for the substrate) becomes crucial to fully understand these coupled phenomena in the multiphysics framework.

An extensive body of work has focused on the development of nonlinear poroelastic theories for gels (Hong et al., 2008; Chester and Anand, 2010), and corresponding mixed finite element frameworks (Lucantonio et al., 2013; Chester et al., 2015; Bouklas et al., 2015; MacMinn et al., 2016), ensuring satisfaction of the Ladyzhenskaya–Babuška–Brezzi (LBB) condition (Babuška, 1971; Brezzi, 1974; Murad and Loula, 1994; Bathe, 2001). Existing frameworks by Javili and Steinmann (2009, 2010) address finite deformation with surface elasticity, and subsequent extensions by McBride et al. (2011); Steinmann et al. (2012) encompass various coupled problems. Several recent works have also followed onto this topic coupling poroelasticity with surface processes (Ang et al., 2020; Kim et al., 2023b,a). Here, we uniquely present a theoretical and computational framework coupling surface diffusion kinetics with the deformation of an impermeable viscoelastic substrate, and perform numerical experiments in the context of surface diffusion in response to substrate deformation.

Our study unveils multiphysical complexities not typically addressed in the previous studies. This complexity arises from the intricate coupling of surface poroelasticity and bulk viscoelasticity. The validity of our theoretical predictions is established through three distinct numerical experiments, offering valuable insights into both viscoelastic and poroelastic relaxation driven by bulk, and surface mechanisms. The manuscript is organized as follows: In Section 2, we describe the coupled theory, encompassing kinematics, balance laws, and the general form of constitutive equations considering both bulk and surface energetics. In Section 3, we specialize the free energies for a poroelastic hydrogel film and a viscoelastic substrate. Section 4 details the finite element implementation, including the weak form, normalization, and solution procedure. Section 5 elaborates the numerical simulations for three boundary value problems: (i) uniaxial tension of a cylindrical bar highlighting the effect of a tension-driven deformation of a substrate, (ii) response under bending showcasing the competing contributions of compression and tension along with competing surface diffusion pathways, and (iii) a rigid sphere indentation of a film/substrate system. Finally, Section 6 provides conclusions and outlines the future research directions.

2. A coupled continuum theory for non-equilibrium processes

2.1. Kinematics

We use the notation $\varphi : (V, t) \rightarrow v$ for the deformation of body \mathcal{B} (see Figure 1). A motion φ is the vector field of the mapping $\mathbf{x} = \varphi(\mathbf{X}, t)$, of a material point in the reference configuration $\mathbf{X} \in V$ to a position in the deformed configuration $\mathbf{x} \in v$. The kinematics of a typical particle are described by the displacement vector field in the spatial description, $\mathbf{u}(\mathbf{X}, t) = \mathbf{x}(\mathbf{X}, t) - \mathbf{X}$. The kinematics of an infinitesimal bulk element are described by

$$\mathbf{F}(\mathbf{X}, t) = \frac{\partial \varphi(\mathbf{X}, t)}{\partial \mathbf{X}} = \nabla_{\mathbf{X}} \varphi(\mathbf{X}, t) \quad (2.1a)$$

$$\mathbf{F}^{-1}(\mathbf{x}, t) = \frac{\partial \varphi^{-1}(\mathbf{x}, t)}{\partial \mathbf{x}} = \nabla_{\mathbf{x}} \varphi^{-1}(\mathbf{x}, t) \quad (2.1b)$$

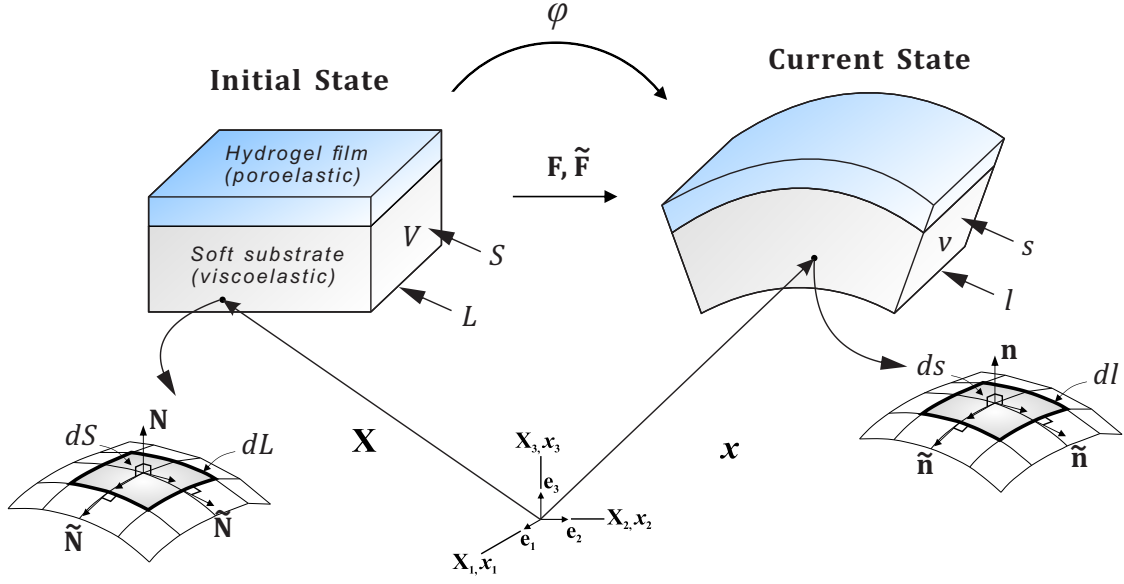


Figure 1: Schematic illustration of the initial and current states of a continuum body. The bulk and surface deformation gradients are denoted by \mathbf{F} and $\tilde{\mathbf{F}}$, respectively. The initial volume and surface, and boundary are denoted by V and S , and L respectively. The current volume and surface, and boundary are denoted by v and s , and l respectively. The normal vector to the surface in the reference and current configuration (\mathbf{N} and \mathbf{n}) and the bi-normal vector to the boundary ($\tilde{\mathbf{N}}$ and $\tilde{\mathbf{n}}$) are shown, where the over-tilde indicates surface quantities.

where $\mathbf{F}(\mathbf{X}, t)$ and $\mathbf{F}^{-1}(\mathbf{x}, t)$ are the deformation gradient and inverse deformation gradient, respectively. Note that $J(\mathbf{X}, t) = dv/dV = \det \mathbf{F}(\mathbf{X}, t) > 0$ is the Jacobian determinant of the deformation gradient defining the ratio of a volume element between the material and spatial configuration. We decompose the deformation gradient into a volumetric and an isochoric part (Flory, 1961; Holzapfel et al., 2000).

$$\mathbf{F} = (J^{1/3} \mathbf{I}) \cdot \bar{\mathbf{F}} \quad (2.2)$$

where $J^{1/3} \mathbf{I}$ and $\bar{\mathbf{F}}$ represent the volumetric and isochoric parts of the deformation gradient \mathbf{F} , and $\{ \cdot \}$ denotes the dot product. Following, we utilize $\{ \bar{\cdot} \}$ to denote quantities associated with the isochoric part of the deformation.

In the context of displacement conformity on surface, the surface displacement can be determined by $\mathbf{u}(\mathbf{X}, t)|_S = \tilde{\mathbf{u}}(\tilde{\mathbf{X}}, t)$. When describing the motion of an arbitrary infinitesimal vector element $d\mathbf{X}$, it is mapped by the deformation gradient \mathbf{F} to a vector $d\mathbf{x}$ in the deformed configuration. However, it is important to note that the transformation of a unit normal vector \mathbf{N} from the material configuration to a unit normal vector \mathbf{n} in the spatial configuration cannot be accomplished using the deformation gradient (Holzapfel, 2000; Steinmann, 2008). This distinction leads us to follow the kinematics of an infinitesimal surface element (Kim et al., 2020, 2023a).

$$\tilde{\mathbf{F}}(\tilde{\mathbf{X}}, t) = \frac{\partial \varphi(\tilde{\mathbf{X}}, t)}{\partial \tilde{\mathbf{X}}} \cdot \tilde{\mathbf{I}} = \tilde{\nabla}_{\tilde{\mathbf{X}}} \varphi(\tilde{\mathbf{X}}, t) \quad (2.3a)$$

$$\tilde{\mathbf{F}}^{-1}(\tilde{\mathbf{x}}, t) = \frac{\partial \varphi^{-1}(\tilde{\mathbf{x}}, t)}{\partial \tilde{\mathbf{x}}} \cdot \tilde{\mathbf{i}} = \tilde{\nabla}_{\tilde{\mathbf{x}}} \varphi^{-1}(\tilde{\mathbf{x}}, t) \quad (2.3b)$$

where $\tilde{\mathbf{F}}(\tilde{\mathbf{X}}, t)$ and $\tilde{\mathbf{F}}^{-1}(\tilde{\mathbf{x}}, t)$ are the surface deformation gradient and inverse surface deformation gradient, and $\tilde{\mathbf{I}} = \mathbf{I} - \mathbf{N} \otimes \mathbf{N}$ and $\tilde{\mathbf{i}} = \mathbf{i} - \mathbf{n} \otimes \mathbf{n}$ are the mixed surface unit tensors with the outward unit normal vectors \mathbf{N} and \mathbf{n} . Note that $\tilde{\mathbf{I}}$ and $\tilde{\mathbf{i}}$ serve as surface (idempotent) projection tensors in the material and spatial configurations, respectively. Furthermore, $\tilde{\mathbf{F}}$ represents a mapping from the bulk (3D) to the surface (2D), resulting in a rank-deficient tensor. Additionally, $\tilde{J}(\tilde{\mathbf{X}}, t) = da/dA = \det \tilde{\mathbf{F}}(\tilde{\mathbf{X}}, t) > 0$ denotes the Jacobian determinant of the surface deformation gradient. This determinant defines the area ratio of a surface element between the material and spatial configurations. We

introduce \mathbf{C} and $\tilde{\mathbf{C}}$, the right Cauchy-Green tensors in the bulk and on the surface, respectively, as

$$\mathbf{C} = \mathbf{F}^T \cdot \mathbf{F} \quad (2.4a)$$

$$\tilde{\mathbf{C}} = \tilde{\mathbf{F}}^T \cdot \tilde{\mathbf{F}} \quad (2.4b)$$

and $I_1 = \text{tr}(\mathbf{C})$ is the first principal invariant. The detailed derivation for the surface kinematics can be found in Green and Zerna (1992); Steinmann (2008); Do Carmo (2016). Note that we cannot perform the inverse of the surface right Cauchy-Green tensor due to its rank deficiency. Nevertheless, we can still obtain its inverse form in the generalized sense,

$$\tilde{\mathbf{C}}^{-1} = \tilde{\mathbf{I}} \cdot \mathbf{C}^{-1} \cdot \tilde{\mathbf{I}} \quad (2.5)$$

which will play a crucial role in our forthcoming developments as it will be utilized to define the surface kinetic law.

2.2. Mechanical equilibrium

Mechanical equilibrium is assumed to be maintained throughout bulk and surface motion at all times. The governing equation for this condition in strong form is as follows:

$$\nabla_{\mathbf{x}} \cdot \mathbf{P} + \mathbf{B} = 0 \quad \text{in } V \quad (2.6a)$$

$$\mathbf{P} \cdot \mathbf{N} - \tilde{\nabla}_{\tilde{\mathbf{x}}} \cdot \tilde{\mathbf{P}} = \mathbf{T} \quad \text{on } S_T \quad (2.6b)$$

$$\mathbf{u} = \mathbf{u}_p \quad \text{on } S_u \quad (2.6c)$$

$$[[\tilde{\mathbf{P}} \cdot \tilde{\mathbf{N}}]] = 0 \quad \text{on } L \quad (2.6d)$$

where \mathbf{P} and $\tilde{\mathbf{P}}$ are the first Piola-Kirchoff stresses in bulk and on surface, \mathbf{B} and \mathbf{T} are the body force and the traction vector, and \mathbf{u}_p is the prescribed displacement. S_T and S_u are the boundary surfaces where traction and displacement are prescribed, respectively. Note that a Neumann-type boundary condition is also defined on boundary curves that $[[\bullet]]$ indicates summation over surfaces intersecting on boundary curves (Kim et al., 2023b).

2.3. Species balance

Here we consider species balance only on the deforming surface of the system, as we consider that the bulk is impermeable, thus we follow only surface diffusion kinetics. Through species (or mass) balance, the strong form for the corresponding governing equation is (McBride et al., 2011; Kim et al., 2023b):

$$\dot{\tilde{C}} + \tilde{\nabla}_{\tilde{\mathbf{x}}} \cdot \tilde{\mathbf{J}} = \tilde{i} \quad \text{on } S_{\tilde{C}} \quad (2.7a)$$

$$\tilde{\mathbf{J}} = \tilde{\mathbf{J}}_p \quad \text{on } L_{\tilde{\mathbf{J}}} \quad (2.7b)$$

$$[[\tilde{\mathbf{J}} \cdot \tilde{\mathbf{N}}]] = 0 \quad \text{on } L \quad (2.7c)$$

where \tilde{C} represents the surface nominal concentration, which is the number of solvent moles per unit reference area. The term $\tilde{\mathbf{J}}$ stands for the surface nominal flux, denoting the number of solvent moles per unit time per unit reference length. The source/sink term is denoted as \tilde{i} . Equation (2.7a) describes the species balance on the surface, and for our model, we assume $\tilde{i} = 0$, signifying that species are conserved. This implies that species neither enter the surface from the external environment nor exit from the interior bulk. In Equation (2.7b), $\tilde{\mathbf{J}}_p$ is the prescribed value on the given boundary curve. $S_{\tilde{C}}$ is the boundary surface where the species are balanced, and $L_{\tilde{\mathbf{J}}}$ is the boundary curve where the surface flux is prescribed. Additionally, these equations are supplemented with initial conditions.

$$\tilde{C}(\tilde{\mathbf{X}}, t = 0) = \tilde{C}_0 \quad (2.8)$$

where \tilde{C}_0 is the initial species concentration on the surface at time $t = 0$. Here we have to note, that as the substrate (the bulk) is impermeable, the terms that couple bulk and surface diffusion in the species balance in (Kim et al., 2023b) have been neglected here, so 2.7 is a reduced form of the species balance presented in that work. We note that we assume that the film/substrate system is embedded in a system in which there is no exchange of solvent with the environment.

2.4. Thermodynamic considerations

We consider the free energy density for both bulk and surface, where we assume that the bulk free energy depends on deformation and viscous dissipation, while the surface free energy is function of deformation and species concentration (Holzapfel et al., 2000). On the other hand, since we are focusing on surface diffusion, the surface free energy can be decomposed into elastic and mixing parts (Hong et al., 2008), as follows

$$\Psi(\mathbf{F}, \mathbf{A}) \quad \text{and} \quad \tilde{\Psi}(\tilde{\mathbf{F}}, \tilde{\mathbf{C}}) \quad (2.9)$$

where \mathbf{A} is an internal variable (second-order tensor) to account for the dissipation process related to the viscoelastic deformation.

Considering a system that includes a viscoelastic substrate and a rigidly bonded porous film with species that can freely migrate within the porous network, the rate of change of the system's free energy \mathcal{G} has to account for several effects (Holzapfel, 2000; Gurtin et al., 2010; Hong et al., 2008; Kim et al., 2023b). This can be expressed as

$$\dot{\mathcal{G}} = \int_V \dot{\Psi} dV + \int_S \dot{\tilde{\Psi}} dS - \int_V \mathbf{B} \cdot \dot{\mathbf{x}} dV - \int_S \mathbf{T} \cdot \dot{\mathbf{x}} dS - \int_S \tilde{\mu} \dot{i} dS \quad (2.10)$$

where the third and fourth terms are the rate of mechanical work by the body force \mathbf{B} and traction vector \mathbf{T} , and the fifth term is the rate of chemical work by the surface chemical potential $\tilde{\mu}$. Note that thermodynamics dictate that the free energy of the system should not increase ($\dot{\mathcal{G}} \leq 0$), and we here consider two dissipation processes: viscous deformation of substrate and the solvent diffusion on film.

Substituting Equation (2.6) and Equation (2.7) into Equation (2.10), the rate of change of the free energy of the system can be expressed as follows,

$$\dot{\mathcal{G}} = \int_V \dot{\Psi} dV + \int_S \dot{\tilde{\Psi}} dS - \int_V \mathbf{P} : \dot{\mathbf{F}} dV - \int_S \tilde{\mathbf{P}} : \dot{\tilde{\mathbf{F}}} dS - \int_S \tilde{\mu} \dot{\tilde{\mathbf{C}}} dS + \int_S \tilde{\mathbf{J}} \cdot \tilde{\nabla}_{\tilde{\mathbf{x}}} \tilde{\mu} dS \leq 0 \quad (2.11)$$

where $\{ : \}$ denotes the double contraction. Using the chain-rule, the rate of bulk and surface free energy densities can be expressed as

$$\dot{\Psi} = \frac{\partial \Psi}{\partial \mathbf{F}} : \dot{\mathbf{F}} + \frac{\partial \Psi}{\partial \mathbf{A}} : \dot{\mathbf{A}} \quad \text{and} \quad \dot{\tilde{\Psi}} = \frac{\partial \tilde{\Psi}}{\partial \tilde{\mathbf{F}}} : \dot{\tilde{\mathbf{F}}} + \frac{\partial \tilde{\Psi}}{\partial \tilde{\mathbf{C}}} : \dot{\tilde{\mathbf{C}}} \quad (2.12)$$

By substituting Equation (2.12) into Equation (2.11), and rearranging terms yields

$$\dot{\mathcal{G}} = \int_V \left(\frac{\partial \Psi}{\partial \mathbf{F}} - \mathbf{P} \right) : \dot{\mathbf{F}} dV + \int_S \left(\frac{\partial \tilde{\Psi}}{\partial \tilde{\mathbf{F}}} - \tilde{\mathbf{P}} \right) : \dot{\tilde{\mathbf{F}}} dS + \int_S \left(\frac{\partial \tilde{\Psi}}{\partial \tilde{\mathbf{C}}} - \tilde{\mu} \right) \dot{\tilde{\mathbf{C}}} dS + \int_S \tilde{\mathbf{J}} \cdot \tilde{\nabla}_{\tilde{\mathbf{x}}} \tilde{\mu} dS + \frac{\partial \Psi}{\partial \mathbf{A}} : \dot{\mathbf{A}} \leq 0 \quad (2.13)$$

where each integral represents a distinct mechanism of energy dissipation, associated with mechanical and chemical works. The inequality must hold at every point of the continuum body and at all times during a thermodynamic process. To satisfy the constraint, the Coleman-Noll procedure (Holzapfel, 2000) states that each integrand in Equation (2.13) to be either negative or equal to zero.

From the first three terms in Equation (2.13) we obtain the following constitutive relations

$$\mathbf{P} = \frac{\partial \Psi(\mathbf{F}, \mathbf{A})}{\partial \mathbf{F}}, \quad \tilde{\mathbf{P}} = \frac{\partial \tilde{\Psi}(\tilde{\mathbf{F}}, \tilde{\mathbf{C}})}{\partial \tilde{\mathbf{F}}} \quad \text{and} \quad \tilde{\mu} = \frac{\partial \tilde{\Psi}(\tilde{\mathbf{F}}, \tilde{\mathbf{C}})}{\partial \tilde{\mathbf{C}}} \quad (2.14)$$

for the bulk and surface first Piola-Kirchhoff stresses tensors, and the surface chemical potentials, respectively.

Additionally, to maintain that the fourth term in Equation (2.13) remains to be negative or zero, we adopt kinetic laws for diffusion (Kim et al., 2023b) on surface. This allows us to maintain negative semi-definiteness and describes the consistent species diffusion that is driven by gradients of chemical potential:

$$\tilde{\mathbf{J}} = -\tilde{\mathbf{M}} \cdot \tilde{\nabla}_{\tilde{\mathbf{x}}} \tilde{\mu} \quad (2.15)$$

Here, $\tilde{\mathbf{M}}$ stands for the surface mobility tensor, which we will later specialize to fully define the constitutive laws governing solvent flux on surface.

Finally, the non-equilibrium thermodynamic process, the last term in Equation (2.13) is characterized by the internal variable for viscoelastic response.

$$\frac{\partial \Psi}{\partial \mathbf{A}} : \dot{\mathbf{A}} \leq 0 \quad (2.16)$$

In the subsequent section, we will specify the evolution of the internal variable $\dot{\mathbf{A}}$ to define the constitutive relations for viscoelastic deformation of substrate.

3. Specific material model

In this study, we make specific selections for the surface and bulk free energy densities, along with their corresponding constitutive laws and the definition of mobility tensors. Our focus is on a compressible viscoelastic substrate, and a hydrogel film that is rigidly bonded and allows surface diffusion kinetics coupled with its deformation.

3.1. Bulk free energy density for soft substrate

We consider the decomposition of the bulk free energy into elastic and viscoelastic components, denoted as $\Psi(\mathbf{F}, \mathbf{A}) = \Psi_e(\mathbf{F}) + \Psi_v(\bar{\mathbf{F}}, \mathbf{A})$. For the elastic part, we employ the compressible hyperelastic model for the bulk free energy density, which has been well-documented in previous work (Holzapfel et al., 2000; Bouklas et al., 2015; Kim et al., 2023b). Regarding the viscoelastic part, we adopt the viscoelastic model proposed by (Linder et al., 2011). This choice allows us to account for the viscoelastic behavior of the material within our formulation.

$$\Psi_e(\mathbf{F}) = \frac{G}{2}(I_1 - 3 - 2 \ln J) + \frac{K}{2}(J - 1)^2 \quad (3.1a)$$

$$\Psi_v(\mathbf{F}, \mathbf{A}) = \frac{G_v}{2}(\mathbf{A} : \bar{\mathbf{C}} - 3 - \ln(\det \mathbf{A})) \quad (3.1b)$$

where G and K are the shear and bulk moduli, and G_v is the viscous modulus for the substrate. It is worth emphasizing that the viscoelastic free energy density Ψ_v depends on two key variables: (i) The modified right Cauchy-Green tensor $\bar{\mathbf{C}} = \bar{\mathbf{F}}^T \bar{\mathbf{F}}$, which indicates that the material's volumetric response remains fully elastic. (ii) The internal variable \mathbf{A} , which describes the material's relaxation behavior and encompasses viscoelastic effects.

3.2. Surface free energy density for hydrogel film

Building upon the approach presented in McBride et al. (2011); Lucantonio et al. (2013, 2016); Kim et al. (2023b,a), we decompose the surface free energy density of the polymer film into two distinct components: $\tilde{\Psi}(\bar{\mathbf{F}}, \bar{\mathbf{C}}) = \tilde{\Psi}_e(\bar{\mathbf{F}}) + \tilde{\Psi}_m(\bar{\mathbf{C}})$. While the standard Flory free energy (Flory and Rehner Jr, 1943; Flory, 1953, 1961) is typically defined with respect to a dry configuration, our study considers a freely swollen hydrogel attached to the substrate as the initial state. Consequently, the homogeneous and isotropic initial swelling should be taken into account to describe the hydrogel film and substrate simultaneously (see also Figure 1).

$$\tilde{\Psi}_e(\bar{\mathbf{F}}) = \frac{1}{\bar{J}_0} \frac{\tilde{G}}{2} \left[\tilde{\lambda}_0^2 \tilde{I}_1 - 2 - 2 \ln(\tilde{J}_0 \tilde{J}) \right] \quad (3.2a)$$

$$\tilde{\Psi}_m(\bar{\mathbf{C}}) = -\frac{\tilde{\beta}}{\bar{J}_0} \frac{k_B T}{\tilde{\Omega}} \left[\tilde{\Omega} \tilde{J}_0 \tilde{C} \ln \left(\frac{1 + \tilde{\Omega} \tilde{J}_0 \tilde{C}}{\tilde{\Omega} \tilde{J}_0 \tilde{C}} \right) + \frac{\tilde{\chi}}{1 + \tilde{\Omega} \tilde{J}_0 \tilde{C}} \right] \quad (3.2b)$$

where $\tilde{\Psi}_e$ and $\tilde{\Psi}_m$ are the free energy densities per unit area at initial (swollen) state, and $\tilde{\lambda}_0$ and \tilde{J}_0 are initial stretch and Jacobian determinant of the surface deformation gradient with respect to the dry configuration of the film. We note that since the film is attached free-swollen (in a planar fashion) to the solid, the general description of the kinematics is about that state, and not the dry state of the film. Nevertheless, for the free energy of the film we need to account the initial swelling (for notation clarity, a detailed discussion can be found in Appendix A). $\tilde{G} = \tilde{N} k_B T$ denotes the surface shear modulus at dry state, where \tilde{N} is the number of polymer chains on the film hydrogel per unit area, k_B is the Boltzmann's constant, and T is an absolute temperature. $\tilde{\Omega}$ corresponds to the area occupied by a solvent molecule on the surface, and $\tilde{\chi}$ is a surface Flory parameter quantifying the degree of polymer-solvent mixing. The parameter

$\tilde{\beta}$ is introduced to account for the number of 2D layers in the surface zone. For a detailed discussion of $\tilde{\beta}$, please refer to our previous work (Kim et al. (2023b), Remark 2).

Following (Hong et al., 2008; Kim et al., 2023b), we assume that the polymer chains and the diffusion species are individually incompressible. The hydrogel, being a condensed matter with negligible void space, experiences area changes primarily due to species diffusion. The species diffusion in thin hydrogel films is assumed to be primarily governed by changes in surface area, focusing on diffusion through the film layer and neglecting the thickness direction. Additionally, at the initial state, the hydrogel contains the initial concentration of the solvent, leading to the following assumptions:

$$1 + \tilde{\Omega}\tilde{C}_0 = \tilde{J}_0 \quad \text{and} \quad 1 + \tilde{\Omega}(\tilde{C} - \tilde{C}_0) = \tilde{J} \Rightarrow \tilde{C} = \tilde{C}_0 + \frac{\tilde{J} - 1}{\tilde{\Omega}} \quad (3.3)$$

where the initial concentration \tilde{C}_0 is determined by the initial stretch $\tilde{\lambda}_0$ that can be determined by the initial chemical potential $\tilde{\mu}_0$, and their analytical expression can be found in Appendix A.

3.3. Evolution equation for viscoelasticity

To fully define the constitutive relation for the viscoelastic response as described in Equation (2.14), governing the free energy relaxation in Equation (2.16), we specify the evolution of internal variable \mathbf{A} as follows by (Linder et al., 2011) and has also been utilized in (Fontenele and Bouklas, 2023).

$$\dot{\mathbf{A}} = \frac{1}{\tau_r} (\bar{\mathbf{C}}^{-1} - \mathbf{A}), \quad \mathbf{A}(\mathbf{X}, t_0) = \mathbf{I} \quad (3.4)$$

where τ_r is the characteristic time scale of relaxation. When $\bar{\mathbf{C}}^{-1} = \mathbf{A}$ is satisfied, it indicates that the system reaches equilibrium and the viscoelastic response is fully relaxed.

3.4. Constitutive equations

Since the chemical boundary conditions for hydrogels are often specified in terms of chemical potential or diffusion flux (proportional to the gradient of chemical potential), it is convenient to use the chemical potential (instead of solvent concentration) as an independent variable in the finite element formulation. Additionally, this allows us to avoid C^1 continuity requirements (Bouklas et al., 2015). For this purpose, we rewrite the free energy densities as a function of the deformation gradient and chemical potential through a Legendre transform (Hong et al., 2008, 2009; Kim et al., 2023b), which replaces a variable with its thermodynamic conjugate:

$$\tilde{\Psi}(\tilde{\mathbf{F}}, \tilde{\mu}) = \tilde{\Psi}(\tilde{\mathbf{F}}, \tilde{C}) - \frac{\tilde{\beta}}{\tilde{J}_0} \tilde{\mu} \tilde{C} \quad (3.5)$$

After the Legendre transform, similar to Equation (2.14), the constitutive relations can be rewritten as follows:

$$\mathbf{P} = \frac{\partial \Psi(\mathbf{F}, \mathbf{A})}{\partial \mathbf{F}}, \quad \tilde{\mathbf{P}} = \frac{\partial \tilde{\Psi}(\tilde{\mathbf{F}}, \tilde{\mu})}{\partial \tilde{\mathbf{F}}} \quad \text{and} \quad \tilde{C} = -\frac{\partial \tilde{\Psi}(\tilde{\mathbf{F}}, \tilde{\mu})}{\partial \tilde{\mu}} \quad (3.6)$$

which the surface first Piola-Kirchhoff $\tilde{\mathbf{P}}$ should be modified because the incompressibility condition was enforced by Equation (3.3) (Hong et al., 2009). The derivation of the surface first Piola-Kirchhoff stress can be found in Appendix A. Using Equations (3.1), (3.2) and (3.6), the specific constitutive relations are obtained as follows:

$$\mathbf{P} = G(\mathbf{F} - \mathbf{F}^{-T}) + K(J - 1)J\mathbf{F}^{-T} + G_v J^{-2/3} \mathbf{F} \cdot \left[\mathbf{A} - \frac{1}{3}(\mathbf{A} : \mathbf{C})\mathbf{C}^{-1} \right] \quad (3.7a)$$

$$\tilde{\mathbf{P}} = \frac{\tilde{G}}{\tilde{J}_0} (\tilde{\lambda}_0^2 \tilde{\mathbf{F}} + \tilde{\alpha} \tilde{J} \tilde{\mathbf{F}}^{-T}), \quad \tilde{\alpha} = -\frac{1}{\tilde{J}} + \frac{\tilde{\beta}}{N\tilde{\Omega}} \left[\tilde{J}_0 \ln \left(1 - \frac{1}{\tilde{J}_0 \tilde{J}} \right) + \frac{1}{\tilde{J}} + \frac{\tilde{\chi}}{\tilde{J}_0 \tilde{J}^2} - \frac{\tilde{\mu}}{k_B T} \right] \quad (3.7b)$$

$$\tilde{\mu} = \tilde{\beta} k_B T \left[\ln \left(\frac{\tilde{\Omega} \tilde{J}_0 \tilde{C}}{1 + \tilde{\Omega} \tilde{J}_0 \tilde{C}} \right) + \frac{1}{1 + \tilde{\Omega} \tilde{J}_0 \tilde{C}} + \frac{\tilde{\chi}}{(1 + \tilde{\Omega} \tilde{J}_0 \tilde{C})^2} \right] \Rightarrow \tilde{C} = \tilde{C}(\tilde{\mathbf{F}}, \tilde{\mu}) \quad (3.7c)$$

where these are the specific forms of the constitutive relations for the first Piola-Kirchhoff stresses and the chemical potential on the surface. Note that the norm of tensor \mathbf{S} ($\|\mathbf{S}\| = \sqrt{\mathbf{S} : \mathbf{S}}$) is to be employed for stress plots in Section 5. It is important to note that we do not use the constitutive relation of Equation (3.7c), but the incompressibility condition of Equation (3.3) to determine the surface concentration \tilde{C} (Hong et al., 2008; Bouklas et al., 2015).

3.5. Surface diffusion

To complete the constitutive relation for the kinetic law governing surface diffusion in Equation (2.15), we specify the surface mobility tensor as follows:

$$\tilde{\mathbf{M}} = \frac{\tilde{C}\tilde{D}}{k_B T} \tilde{\mathbf{C}}^{-1} \quad (3.8)$$

The diffusion coefficient of the solvent molecules \tilde{D} on the surface are assumed to be isotropic and independent of the deformation and concentration as the simplest approximation (Kim et al., 2023b). Note that the current concentrations are related to the nominal concentrations as $\tilde{c} = \tilde{C}/\tilde{J}$.

4. Mixed finite element formulation

This section outlines the finite element formulation, employing FEniCS for implementation, based on the nonlinear theory presented in Sections 2 and 3 using FEniCS (Logg et al., 2012; Alnæs et al., 2015) for the implementation. The formulation commences with the strong expression of the governing equations, incorporating the initial and boundary conditions. Subsequently, the weak form of the problem is introduced, followed by an explanation of the normalization, discretization, and the steps involved in the solution process. It is important to note that, in this section, we concentrate on the surface diffusion coupled with the deformation of the substrate. As such, we do not consider the source terms, that is, $\tilde{i} = 0$.

4.1. Two-field weak form

The weak form of the problem is obtained by using a set of test functions, which satisfy the necessary integrability conditions (Hughes, 2012). By multiplying Equation (2.6a) and Equation (2.7a) with the test functions $\delta\mathbf{u}$ and $\delta\tilde{\mu}$, and integrating over the domain, respectively, then we obtain that

$$\int_V \mathbf{P} : \nabla_{\mathbf{X}} \delta\mathbf{u} \, dV + \int_S \tilde{\mathbf{P}} : \tilde{\nabla}_{\tilde{\mathbf{X}}} \delta\mathbf{u} \, dS = 0 \quad (4.1a)$$

$$\int_S \tilde{C} \delta\mu \, dS - \int_S \tilde{\mathbf{J}} \cdot \tilde{\nabla}_{\tilde{\mathbf{X}}} \delta\mu \, dS = 0 \quad (4.1b)$$

The statement of the weak form is to find the trial functions, \mathbf{u} and $\tilde{\mu}$, such that the integrals in Equation (4.1) are satisfied for any permissible test functions, $\delta\mathbf{u}$ and $\delta\tilde{\mu}$.

4.2. Normalization

For the finite element simulations in the following section, all variables and parameters are normalized, as denoted by $\{\bullet\}$. All lengths are normalized by a characteristic dimension, $H = \tilde{G}/G$ (shear moduli ratio). The chemical potential and stresses are normalized as follows,

$$\hat{\mathbf{P}} = \frac{\mathbf{P}}{G}, \quad \hat{\tilde{\mathbf{P}}} = \frac{\tilde{\mathbf{P}}}{\tilde{G}}, \quad \hat{\tilde{\mu}} = \frac{\tilde{\mu}}{\beta k_B T} \quad (4.2)$$

Solvent concentration and time are normalized as follows,

$$\hat{\tilde{C}} = \tilde{\Omega} \tilde{C}, \quad \hat{t} = \frac{t}{\tau_d} \quad (4.3)$$

where $\tau_d = \tilde{H}^2/\tilde{D}$ is the characteristic time scale of diffusion.

By substituting the normalized variables into the weak forms in Equation (4.1), we can obtain the normalized weak forms.

$$\int_V \widehat{\mathbf{P}} : \nabla_{\widehat{\mathbf{X}}} \delta \widehat{\mathbf{u}} d\widehat{V} + \int_S \widehat{\mathbf{P}} : \widehat{\nabla}_{\widehat{\mathbf{X}}} \delta \widehat{\mathbf{u}} d\widehat{S} = 0 \quad (4.4a)$$

$$\int_S \frac{d\widehat{\mathbf{C}}}{d\widehat{t}} \delta \widehat{\mu} d\widehat{S} - \int_S \widehat{\mathbf{J}} \cdot \frac{\partial \delta \widehat{\mu}}{\partial \widehat{\mathbf{X}}} d\widehat{S} = 0 \quad (4.4b)$$

where the normalized flux is defined by

$$\widehat{\mathbf{J}} = -\widehat{\mathbf{C}}\widehat{\mathbf{C}}^{-1} \cdot \widehat{\nabla}_{\widehat{\mathbf{X}}} \widehat{\mu} \quad (4.5)$$

4.3. Temporal discretization

To update the species balance, the backward Euler scheme is used to integrate Equation (4.4b) over time:

$$\int_S \left[\frac{1}{\Delta \widehat{t}} (\widehat{\mathbf{C}}^{\widehat{t}+\Delta \widehat{t}} - \widehat{\mathbf{C}}^{\widehat{t}}) \delta \widehat{\mu} - \int_S \widehat{\mathbf{J}}^{\widehat{t}+\Delta \widehat{t}} \cdot \widehat{\nabla}_{\widehat{\mathbf{X}}} \delta \widehat{\mu} \right] d\widehat{S} = 0 \quad (4.6)$$

where the superscripts indicate the time step, at the current time step ($\widehat{t} + \Delta \widehat{t}$) or the previous step \widehat{t} . We can combine Equations (4.4a) and (4.6) as

$$\int_V \widehat{\mathbf{P}} : \nabla_{\widehat{\mathbf{X}}} \delta \widehat{\mathbf{u}} d\widehat{V} + \int_S \widehat{\mathbf{P}} : \widehat{\nabla}_{\widehat{\mathbf{X}}} \delta \widehat{\mathbf{u}} d\widehat{S} + \int_S (\widehat{\mathbf{C}} - \widehat{\mathbf{C}}^{\widehat{t}}) \delta \widehat{\mu} d\widehat{S} + \Delta \widehat{t} \int_S (\widehat{\mathbf{C}}\widehat{\mathbf{C}}^{-1} \cdot \widehat{\nabla}_{\widehat{\mathbf{X}}} \widehat{\mu}) \cdot \widehat{\nabla}_{\widehat{\mathbf{X}}} \delta \widehat{\mu} d\widehat{S} = 0 \quad (4.7)$$

where the superscript ($\widehat{t} + \Delta \widehat{t}$) is omitted for all the terms at the current time step and $\widehat{\mathbf{C}}^{\widehat{t}}$ and $\widehat{\mathbf{C}}^{\widehat{t}}$ are the species concentration at the previous time step in the bulk and on the surface.

Note that, we also adopt the the backward Euler scheme with Equation (3.4) to update the viscoelastic response, resulting in the update of the internal variable \mathbf{A} .

$$\mathbf{A} = \frac{1}{1 + (\tau_d/\tau_r) \Delta \widehat{t}} \left[\mathbf{A}^{\widehat{t}} + (\tau_d/\tau_r) \Delta \widehat{t} \overline{\mathbf{C}}^{-1} \right] \quad (4.8)$$

where the terms without the superscript are at the current time step, and $\mathbf{A}^{\widehat{t}}$ is the internal variable at the previous time step.

4.4. Spatial discretization

A mixed finite element method is employed to concurrently solve for the normalized displacement and surface chemical potential fields. To circumvent potential numerical instabilities associated with the mixed method, appropriate spatial discretization techniques are essential (Kim et al., 2023b,a). In this context, we adopt the Taylor-Hood element (Taylor and Hood, 1973), where the displacement and surface chemical potential are interpolated using quadratic and linear orders, respectively. It is important to note that linear interpolation is only utilized on the surface, where polymeric film is applied.

The normalized displacement and chemical potential are interpolated through the domain of interest as

$$\widehat{\mathbf{u}} = \mathbf{H}^{\widehat{\mathbf{u}}} \widehat{\mathbf{u}}^n, \quad \widehat{\mu} = \mathbf{H}^{\widehat{\mu}} \widehat{\mu}^n \quad (4.9)$$

where $\mathbf{H}^{\widehat{\mathbf{u}}}$, $\mathbf{H}^{\widehat{\mu}}$ and $\widehat{\mathbf{H}}^{\widehat{\mathbf{C}}}$ are the shape functions, $\widehat{\mathbf{u}}^n$, $\widehat{\mu}^n$ and $\widehat{\mathbf{C}}^n$ are the nodal values of the normalized displacement, chemical potential and surface concentration, respectively. Note that the shape function $\widehat{\mathbf{H}}^{\widehat{\mathbf{C}}}$ is only defined on surface elements. The test functions are discretized in the same way

$$\delta \widehat{\mathbf{u}} = \mathbf{H}^{\widehat{\mathbf{u}}} \delta \widehat{\mathbf{u}}^n, \quad \delta \widehat{\mu} = \mathbf{H}^{\widehat{\mu}} \delta \widehat{\mu}^n \quad (4.10)$$

The stresses, concentrations, and fluxes are evaluated at integration points, depending on the gradients of the displacement and chemical potential via the constitutive relations. Taking the gradient of Equation (4.9), we obtain that

$$\nabla_{\widehat{\mathbf{x}}}\widehat{\mathbf{u}} = \nabla_{\widehat{\mathbf{x}}}\mathbf{H}^{\widehat{\mathbf{u}}}\widehat{\mathbf{u}}^n = \mathbf{B}^{\widehat{\mathbf{u}}}\widehat{\mathbf{u}}^n \quad (4.11a)$$

$$\nabla_{\widehat{\mathbf{x}}}\widehat{\mu} = \nabla_{\widehat{\mathbf{x}}}\mathbf{H}^{\widehat{\mu}}\widehat{\mu}^n = \mathbf{B}^{\widehat{\mu}}\widehat{\mu}^n \quad (4.11b)$$

where $\mathbf{B}^{\widehat{\mathbf{u}}}$ and $\mathbf{B}^{\widehat{\mu}}$ are the gradients of the shape functions in the bulk.

4.5. Nonlinear solution

The weak form in Equation (4.7) can be expressed as a system of nonlinear equations,

$$\mathcal{N}(\mathbf{d}) = \mathbf{f} \quad \text{with} \quad \mathbf{d} = [\widehat{\mathbf{u}}^n \widehat{\mu}^n]^T \quad (4.12)$$

Note that $\mathcal{N}(\mathbf{d})$ denotes the part of the weak form that is not known at current time step, and we take all the known quantities to the right-hand side and denote as \mathbf{f} (which is known from previous time step). The residual of nonlinear equations in iteration step i is given by $\mathbf{R}_i = \mathbf{f} - \mathcal{N}(\mathbf{d}_i)$, which can be solved using the Newton–Raphson method. In particular, the procedure requires the calculation of the tangent Jacobian matrix at each iteration, namely,

$$\left. \frac{\partial \mathcal{N}}{\partial \mathbf{d}} \right|_{\mathbf{d}_i} = \begin{bmatrix} \mathbf{K}^{\widehat{\mathbf{u}}\widehat{\mathbf{u}}} & \mathbf{K}^{\widehat{\mathbf{u}}\widehat{\mu}} \\ \mathbf{K}^{\widehat{\mu}\widehat{\mathbf{u}}} & \mathbf{K}^{\widehat{\mu}\widehat{\mu}} \end{bmatrix} \quad (4.13)$$

FEniCS version 2019.2.0 (Logg et al., 2012; Alnæs et al., 2015) is used to numerically solve the coupled non-linear equations via the Portable Extensible Toolkit for Scientific Computations (PETSc) Scalable Nonlinear Equations Solvers (SNES) interface (Balay et al., 2019). This process repeats until a level of convergence specified within the SNES solver. At each iteration, the block Jacobian matrices are set up using multiphenics (Ballarin, 2019), a python library that also facilitates the definition of boundary restricted variables within FEniCS, a feature necessary for dealing in our case with the surface concentration. We note that the surface displacement is tied with the definition of the corresponding bulk displacement, but the surface concentration is not.

5. Numerical examples

We explore the transient responses of three initial and boundary value problems, involving the viscoelasticity of a soft substrate and the surface diffusion of a hydrogel thin film (see Figure 1 for general setup). The numerical studies include: (1) uniaxial tension of a cylindrical bar, (2) bending of a rectangular beam, and (3) rigid sphere indentation of a planar film/substrate system. In these examples, we consider $k_B T = 4 \times 10^{-21}$ J/mol. For the soft substrate, the shear and bulk moduli are set as $G = 1.0$ N/m² and $K = 2.16$ N/m², leading to a Poisson’s ratio of $\nu = 0.3$. Additionally, the viscous modulus is considered as $G_v = 1.0$ N/m². Note that we intentionally select a relatively large G_v to highlight the influence of viscoelasticity. Regarding the hydrogel film, the surface shear modulus at dry state is assumed to be $\widetilde{G} = 10^{-2}$ N/m, and characteristic dimensions of $H = 10^{-2}$ m and $\widetilde{N}\Omega/\beta = 10^{-3}$ (dimensionless). Finally, we simplify the numerical examples by setting the characteristic time scale as $\tau := \tau_d = \tau_r = 1.0$ sec.

To investigate the transient response that follows mechanical loading, we employ a two-stage process. In the first stage, we linearly ramp the displacement boundary condition from zero to its prescribed value within the time interval $t/\tau \in [0.0, 0.01]$. This interval is deliberately set small, representing only 1% of the characteristic time scale for surface diffusion and viscoelasticity responses. Therefore, in the first stage, the non-equilibrium processes are negligible. In the second stage, we exponentially increase the time steps $\Delta t/\tau$ until equilibrium is attained, while keeping the boundary conditions constant. This longer time step allows us to capture the non-equilibrium processes as time progresses.

The initial state of the hydrogel film is selected based on the the surface Flory parameter $\widetilde{\chi} = 0.7705$ and initial chemical potential $\widehat{\mu}_0 = 0$, indicating a fully swollen state. By solving the non-linear algebraic equation in Equation (A.6), the initial stretch is obtained as $\lambda_0 \approx 1.41$; subsequently, the normalized initial solvent concentration is obtained by $\widetilde{C}_0 \approx 1.0$ using the incompressibility condition in Equation (3.3). It is worth noting that the surface Flory parameter was chosen to make the simulation and interpretation more straightforwardly, particularly with a unit surface concentration at initial state (see Appendix A for detail).

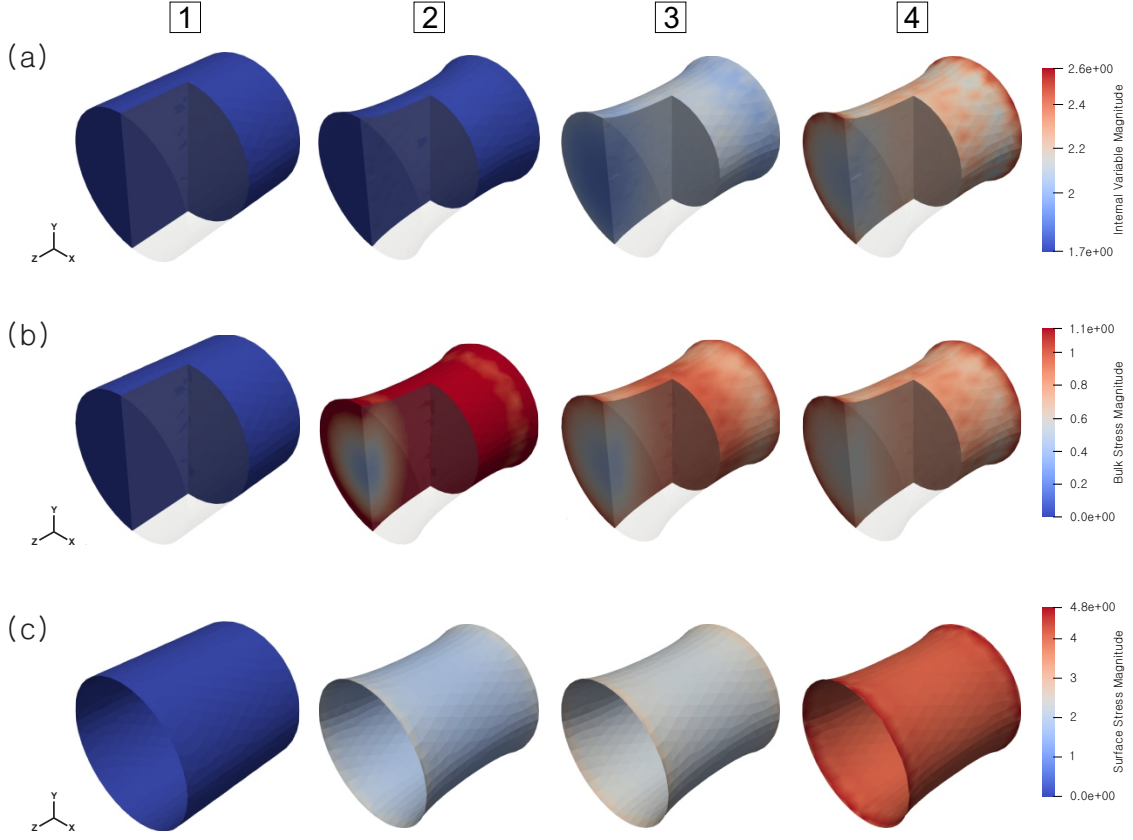


Figure 2: Temporal sequence of (a) internal variable, (b) bulk stress, and (c) surface stress during the tension of a bar, with all variables normalized. The images are captured at normalized times $t/\tau = 0.0, 0.01, 2.0,$ and 1.9×10^6 from left to right, labeled as Step 1, 2, 3, and 4, respectively.

5.1. Uniaxial tension of a cylindrical bar

In this example, we investigate the non-equilibrium response of a soft bar subject to uniaxial tension. At the undeformed state, the radius of cross section is H and the length of the bar is $2H$. The soft bar is considered to be covered by a hydrogel film on its free surface but not on the clamped ends. The two-stage solution procedure detailed above is followed here. One end of the bar is clamped and held fixed, while the other end is clamped and displaced along the axis of the bar. Displacement is prescribed for the first stage of the solution procedure, and held fixed for the remainder. The non-homogeneous deformation profile that the bar attains during loading, is what drives surface diffusion.

In Figure 2, we present the temporal evolution of the finite element simulation for the internal variables, bulk and surface stresses. Simultaneously, in Figure 3, we display the temporal evolution of surface chemical potential, concentration, and flux, with all values normalized. To focus on the contour plot on two sections of the interior along with the field on the surface, we have removed a quarter of the domain from the images of internal variables and bulk stresses in Figure 2(a) and (b). For better visualization of surface fluxes in Figure 3, we show the fluxes on a quarter of the bar. The images are captured at normalized times $t/\tau = 0.0, 0.01, 2.0,$ and 1.9×10^6 from left to right, labeled as Step 1, 2, 3, and 4, respectively, in the following discussion.

In Step 1 of Figures 2 and 3, the bar represents the initial state, where the initial chemical potential is $\widehat{\mu} = 0$, and the concentration is $\widehat{C} = 1$. Step 2 of Figures 2 and 3 corresponds to the time step where the boundary conditions are linearly ramped up to an end-to-end 10% extension. This occurs at time $t/\tau = 0.1$, which is significantly smaller (7 orders of magnitude) compared to the equilibration time at Step 4. As the bar is stretched, both bulk and surface stresses increase (see Step 2 in Figure 2(b) and (c)), and the surface chemical potential decreases (see Step 2 in Figure 3(a)). Although the time steps are very small in Step 2, the surface flux is observed at the boundary edges as a

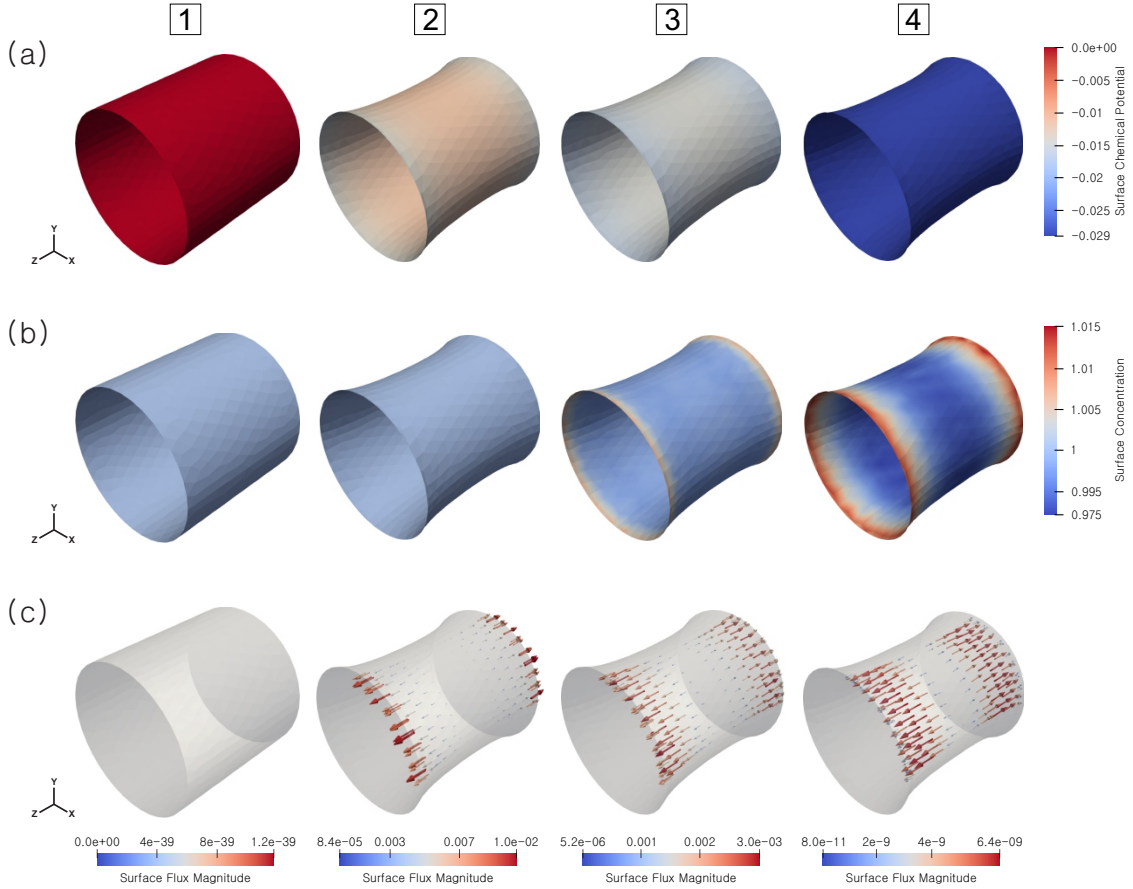


Figure 3: Temporal sequence of (a) surface chemical potential, (b) surface concentration, and (c) surface flux during the tension of a bar, with all variables normalized. The images are captured at normalized times $t/\tau = 0.0, 0.01, 2.0,$ and 1.9×10^6 from left to right, labeled as Step 1, 2, 3, and 4, respectively.

result of the deformation (see Step 2 in Figure 3(c)); however, the time step is so small that the surface concentration is nearly unchanged (see Step 2 in Figure 3(b)).

Beyond Step 2, and for the remainder of the transient response, the displacement boundary condition is held fixed under a 10% overall extension, and we exponentially increases the magnitude of the time steps towards equilibrium. In Step 3, the bar continues to deform primarily due to the viscoelastic relaxation of the substrate, but also due to the surface poroelastic relaxation of the film. Specifically, the internal variable \mathbf{A} increases (Figure 2(a), Step 3), leading to the relaxation of bulk stress (Figure 2(b), Step 3). This relaxation drives the surface flux of the film (Figure 3(c), Step 3) and results in heterogeneous surface concentration (Figure 3(b), Step 3). Interestingly, the surface stress increases (contrary to the stress drop in the bulk) because the film is assumed to not be viscoelastic (Figure 2(c), Step 3). The system reaches its equilibrium state at Step 4. This is confirmed by the homogeneous chemical potential (Figure 3(a), Step 4) and negligible surface flux (Figure 3(c), Step 4).

5.2. Bending of a soft beam

In this example, we explore the non-equilibrium responses under bending conditions. The edge length of the cross-section is set as H , and the length of the bar is $2H$. Unlike the previous example in Section 5.2 where we focused on stretching, here we probe a more complex scenario involving bending. For the boundary conditions, we linearly ramp the displacement boundary condition from zero to its prescribed value within the time interval $t/\tau \in [0.0, 0.01]$. During this interval, both ends of the beam gradually rotate up to 26.56 degree around the center-line, resulting in the upper part of the beam being stretched and the lower part being compressed.

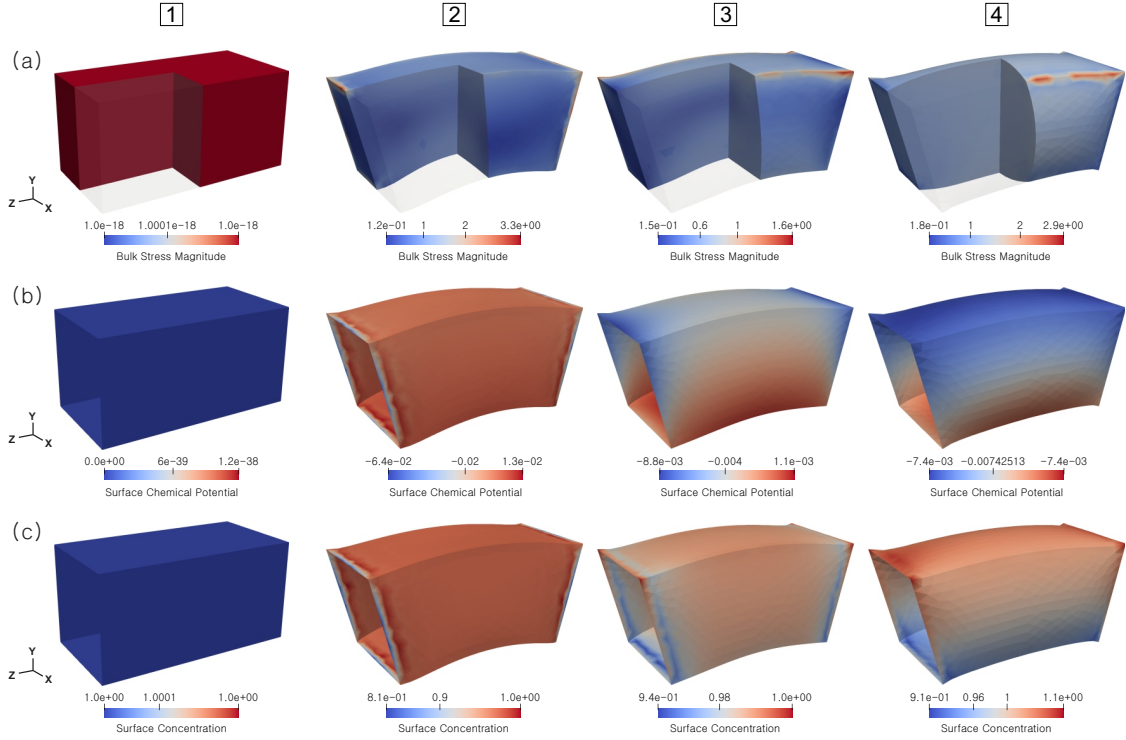


Figure 4: Temporal sequence of (a) bulk stress, (b) surface chemical potential, and (c) surface concentration during the bending of a beam, with all variables normalized. The images are captured at normalized times $t/\tau = 0.0, 0.01, 2.0,$ and 1.9×10^6 from left to right, labeled as Step 1, 2, 3, and 4, respectively.

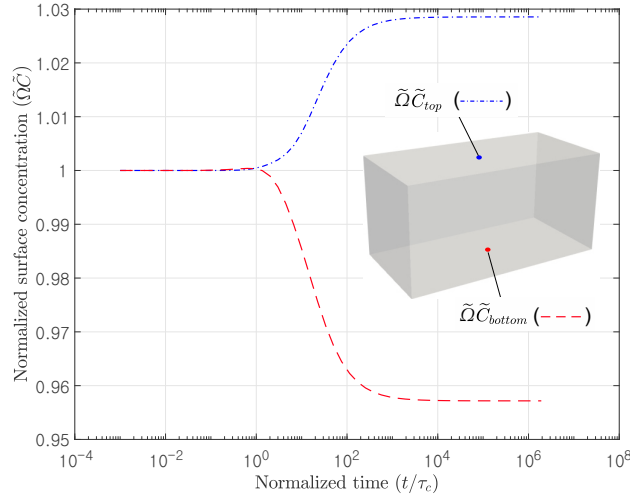


Figure 5: Normalized surface concentrations (\tilde{C}) at top and bottom points tracked over normalized time (t/τ). During the bending of the beam ($t/\tau < 0.01$), the surface concentrations at the top and bottom are nearly the same. However, as the bending progresses, the surface concentration at the top (under tension) increases, while the one at the bottom (under compression) decreases.

In Figure 4, we showcase the temporal evolution of the finite element simulation for bulk surface stress, surface chemical potential, and concentration, with all values normalized. To focus on the contour plot on two sections of the interior along with the field on the surface, we have removed a quarter of the domain from the images of bulk stresses in Figure 4(a). The images are captured at normalized times $t/\tau = 0.0, 0.01, 2.0,$ and 1.9×10^6 from left to right,

labeled as Step 1, 2, 3, and 4, respectively, in the following discussion. In Step 1 of Figure 4, the beams represent the initial states, where the initial conditions remain the same as in the previous example (see Section 5.2). Step 2 of Figure 4 corresponds to the time step where the boundary conditions are linearly ramped up to a 26.56 degree rotation. As the beam bends, bulk stresses increase, particularly at the sharp edges and corners. The surface chemical potential and concentration decrease, but some boundary effects near both ends are observable. The simulation results at Step 2 essentially represent the equilibrium response of the elastic part of the strain energy.

Beyond Step 2, for the remainder of the transient response, the boundary condition is held fixed, and we exponentially increase the time steps toward equilibrium. Throughout the transient analysis, our focus is on observing non-equilibrium responses and their multiphysical complexities. In Step 3, the beam continues to deform beyond the fixed boundary condition, representing the viscoelastic response of free energy relaxation. While observing the relaxation of bulk stress, we interestingly note stress concentration at the corners (Figure 4(a), Step 3). This relaxation leads to the heterogeneous surface chemical potential of the film (Figure 4(c), Step 3) and results in heterogeneous surface concentration (Figure 4(b), Step 3). The non-equilibrium processes persist, and the system reaches the equilibrium state at Step 4. The boundary effect disappears, and we observe an increase in surface concentration in the upper stretched part and a decrease in the lower compressed part. We plot the surface concentration at the top and bottom surfaces, corresponding to the stretched and compressed regions, respectively. Interestingly, the concentrations remain almost the same until $t/\tau \approx 1$, even though the beam is completely bent. However, as the non-equilibrium processes continue, the surface concentration at the top surface increases, and the surface concentration at the bottom surface decreases. This observation emphasizes the impact of the viscoelastic response on surface diffusion.

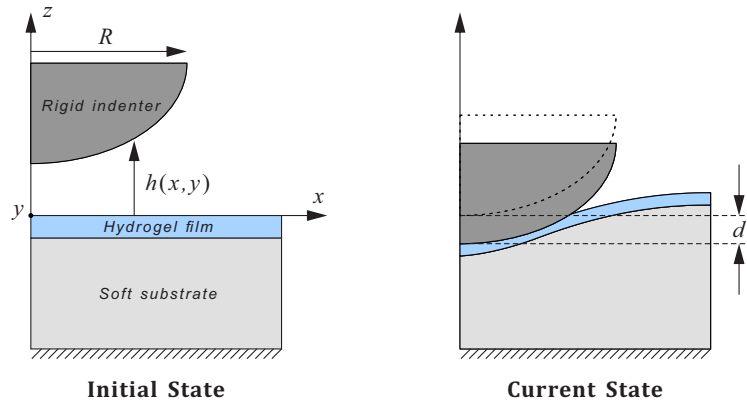


Figure 6: Schematic illustration of the initial and current states of indentation-induced deformation and diffusion in a film-coated soft block. In the initial state, the rigid indenter has a radius R , and its surface is described by $h(x, y)$. In the current state, the rigid indenter pushes the block to a depth of d , resulting in solvent diffusion and inflating deformation.

5.3. Rigid sphere indentation of a film/substrate rectangular block

In various engineering applications, poroelastic gels are often released from patterned molds, exhibiting time-dependent mechanical behavior, due to surface diffusion (Brenner and Leal, 1977; Yang and Srolovitz, 1994) and also viscoelasticity of the substrate (Stafford et al., 2004; Lin et al., 2008; Liu et al., 2021). Motivated by these observations, this example explores the transient response to indentation, indicative of viscoelastic and poroelastic relaxation. The top surface dimensions (x - y plane) are set as an edge length of H , and the height is $H/2$. Regarding boundary conditions, the bottom surface is clamped, and the remaining surfaces are stress-free. Notably, the indenter is not explicitly modeled, but we only consider the surface of the rigid indenter as follows.

$$h(x, y) = h_0 + \frac{1}{2R} (x^2 + y^2) \quad (5.1)$$

Here, h_0 is the initial gap between the top surface and the tip of the rigid indenter. If $h > 0$, there is no contact between both surfaces; contact appears only if $h \leq 0$. We linearly ramp the rigid indentation from zero to its maximum depth $d = 0.1H$ within the time interval $t/\tau \in [0.0, 0.01]$, where the radius of the rigid indenter is $R = 0.2H$ (see Figure 6).

To facilitate this, we use the contact formation with penalty approach, which leads to the pressure p on the contact surface:

$$p = k_p \langle -g \rangle \quad \text{where} \quad g = h - u_z \quad (5.2)$$

Here, $\langle x \rangle = (|x| + x) / 2$ is the Macaulay brackets, k_p is the penalty coefficient, g is the gap, and u_z is the displacement in the direction z . The weak form to account for the contact problem of rigid indentation can be formulated as:

$$\begin{aligned} & \int_V \widehat{\mathbf{P}} : \nabla_{\widehat{\mathbf{x}}} \delta \widehat{\mathbf{u}} dV + \int_S \widehat{\mathbf{P}} : \widehat{\nabla}_{\widehat{\mathbf{x}}} \delta \widehat{\mathbf{u}} dS \\ & + \int_S \left(\widehat{\mathbf{C}} - \widehat{\mathbf{C}}^f \right) \delta \widehat{\boldsymbol{\mu}} dS + \Delta t \int_S \left(\widehat{\mathbf{C}} \mathbf{C}^{-1} \cdot \widehat{\nabla}_{\widehat{\mathbf{x}}} \widehat{\boldsymbol{\mu}} \right) \cdot \widehat{\nabla}_{\widehat{\mathbf{x}}} \delta \widehat{\boldsymbol{\mu}} dS \\ & + \widehat{k}_p \int_{S_{top}} \langle \widehat{u}_z - \widehat{h} \rangle \delta \widehat{u}_z dS = 0 \end{aligned} \quad (5.3)$$

The last term on left-hand side in Equation (5.3) is the penalty formulation for contact problem (Belytschko et al., 2014; Bleyer, 2018), where S_{top} denotes the top surface, and the weak form is normalized with respect to the characteristic length scale H . The normalized penalty coefficient is set as $\widehat{k}_p = 100$, which is sufficiently larger than the material moduli.

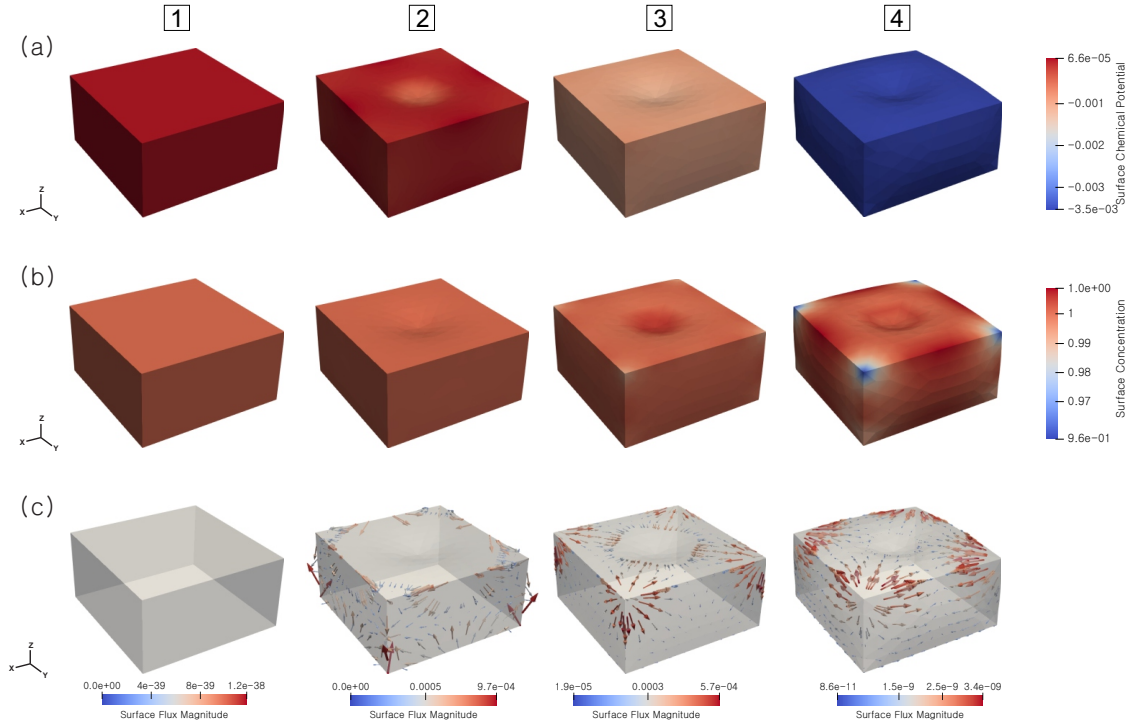


Figure 7: Temporal sequence of (a) surface chemical potential, (b) surface concentration, and (c) surface flux during the indentation, with all variables normalized. The images are captured at normalized times $t/\tau = 0.0, 0.01, 2.0,$ and 1.9×10^6 from left to right, labeled as Step 1, 2, 3, and 4, respectively.

In Figure 7, we showcase the temporal evolution of the finite element simulation for surface chemical potential, concentration and flux, with all values normalized. The images are captured at normalized times $t/\tau = 0.0, 0.01, 2.0,$ and 1.9×10^6 from left to right, labeled as Step 1, 2, 3, and 4, respectively, in the following discussion. In Step 1 of Figure 7, the block represent the initial state, where the initial conditions remain the same as in the previous example (see Section 5.2). Step 2 of Figure 7 corresponds to the time step where rigid indentation reach the prescribed depth.

As the indenter punches the block, surface chemical potential decreases (see Figure 7a), which leads to the small surface flux away from the indentation (see Figure 7c). Note that the time step up to Step 2 is so small that the change of surface concentration is negligible (see Figure 7b).

Beyond Step 2, for the remainder of the transient response, the indentation depth is held fixed, with the rigid indenter kept in position, and we exponentially increase the magnitude of the time steps toward equilibrium. In Step 3, the block continues to deform, representing the viscoelastic response of free energy relaxation. Interestingly, we note that the direction of surface flux becomes opposite, moving away from the corners toward the indented surface (compare Figure 7(c) Step 3 with Step 2). Intuitively, one may expect that the solvent initially flows away from the indentation for a short time, and as the relaxation proceeds, the solvent flows towards the deepest point of indentation. The system reaches the equilibrium state at Step 4, where there is heterogeneous surface concentration and deformed substrate.

6. Conclusion

A comprehensive multiphysics model, integrating surface diffusion, surface elasticity and bulk viscoelasticity, has been introduced and implemented using finite element analysis. The governing equations for non-equilibrium processes in a continuum body are established for surface poroelasticity and bulk viscoelasticity, with constitutive relations derived in a thermodynamically-consistent manner. This formulation is specialized for a hydrogel film and impermeable viscoelastic soft substrate. The numerical solution, is based on a mixed finite element method and implemented using the open-source framework FEniCS.

In the first example, involving the stretching of a cylindrical bar (Figures 2 and 3 in Section 5.1), evolution of internal variables, bulk and surface stresses, surface chemical potential, concentration, and surface flux are examined. Contrary to expectations, the results in Figure 2(c) show that surface stress does not relax similar to bulk stress due to viscoelastic relaxation but has an opposite trend, highlighting the significant role of multiphysical complexities in comprehending the responses of soft solids. The solvent gradually flows toward both clamped ends until equilibrium is attained.

The second example (Figures 4 and 5 in Section 5.2) further investigates the bending of the beam to address the question arising from the first example. While the distributions of surface concentration in Step 2 are similar to those in the first example (compare Figure 3(c) and Figure 4(c)), the second example reveals significant differences in the pathways of species migration. This observation clarifies that non-equilibrium processes (relaxation of bulk stress) could be important in the species distribution on the film.

In the third example (Section 5.3), we delve into the more practical scenario of indentation-driven deformation and diffusion, considering the widespread use of hydrogel films in engineering applications such as sensors, drug delivery systems, and biomedical engineering. In this numerical study (Figure 7), we unveil that in the early stage, the solvent on the film flows away from the indentation, and the substrate deforms only in the indented part. As the transient processes progress, the solvent flows towards the center of the indented area, and the substrate deforms in regions outside the indentation. This interpretation provides crucial insights into applications of hydrogel-based films. For instance, one might utilize the change in species on the film surface for the advanced design of hydrogel-based sensors.

This paper presents three numerical studies to explore the effect of multiphysical processes and their intricate coupling. The key finding is that we uncover the underlying principles through which one could design a system with variable surface concentration of a particular species, by coupling bulk deformation with surface diffusion mechanism. One may leverage these features for the design of advanced soft material-based engineering components. For future work, it would be intriguing to extend our model to consider surface instability mechanisms to account for surface wrinkling and buckling, which could significantly enhance or suppress surface diffusion in a patterned manner.

CRediT authorship contribution statement

Jaemin Kim: Writing - Original Draft, Reviewing and Editing, Conceptualization, Methodology, Software, Validation, Investigation, Visualization. **Keon Ho Kim:** Writing- Reviewing and Editing. **Nikolaos Bouklas:** Writing- Reviewing and Editing.

Acknowledgments

JK received no financial support for the research, authorship, and/or publication of this article. KK acknowledges research support through the Peter O'Donnell Jr. Postdoctoral Fellowship at the Oden Institute for Computational Engineering and Sciences, University of Texas at Austin.

Declarations

The authors declare that they have no known competing financial interests or personal relationships that could have appeared to influence the work reported in this paper.

Appendix A. Derivation of surface stress and algebraic equation for free swelling stretch

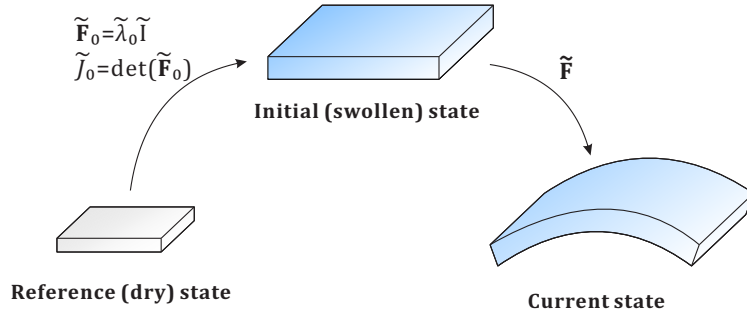


Figure A.8: Schematic illustration of the dry, swollen (initial), and current states of a hydrogel film. The initial state represents the free-swollen hydrogel given the initial chemical potential $\tilde{\mu}_0$, isotropically scaled from the reference state. The stretch and the Jacobian determinant are denoted as $\tilde{\lambda}_0$ and \tilde{J}_0 . The swollen hydrogel is attached to the substrate that is assumed to be initial state (see also Figure 1), and its current state is characterized by the surface deformation gradient $\tilde{\mathbf{F}}$.

In Figure A.8, the homogeneously swollen stress-free (initial) state can be described using the initial stretch ratio $\tilde{\lambda}_0$ and the corresponding deformation gradient $\tilde{\mathbf{F}}_0 = \tilde{\lambda}_0 \tilde{\mathbf{I}}$, with the corresponding Jacobian determinant given by $\tilde{J}_0 = \tilde{\lambda}_0^2$. The deformation of the film on the substrate can be described using surface kinematics denoted by $\tilde{\mathbf{F}}$ (see Figure 1). As the solvent concentration \tilde{C} is defined with respect to the initial (swollen) state, and the solvent concentration with respect to the dry state is given by $\tilde{J}_0 \tilde{C}$. Considering the incompressibility condition of Equation (3.3), we can rewrite the constraint in terms of the reference (dry) state,

$$1 + \tilde{\Omega} \tilde{J}_0 \tilde{C} = \tilde{J}_0 \tilde{J} \quad (\text{A.1})$$

By substituting Equation (A.1) into Equation (3.2) and performing a Legendre transform, the strain energy density at the initial (swollen) state can be written as:

$$\tilde{\Psi}(\tilde{\mathbf{F}}, \tilde{\mu}) = \frac{1}{2} \frac{\tilde{G}}{\tilde{J}_0} \left[\tilde{\lambda}_0^2 \tilde{I}_1 - 2 - 2 \ln(\tilde{J}_0 \tilde{J}) \right] - \frac{\tilde{\beta}}{\tilde{J}_0} \frac{k_B T}{\tilde{\Omega}} \left[\tilde{\Omega} \tilde{J}_0 \tilde{C} \ln \left(\frac{1 + \tilde{\Omega} \tilde{J}_0 \tilde{C}}{\tilde{\Omega} \tilde{J}_0 \tilde{C}} \right) + \frac{\tilde{\chi}}{1 + \tilde{\Omega} \tilde{J}_0 \tilde{C}} \right] - \frac{\tilde{\beta}}{\tilde{J}_0} \tilde{\mu} \tilde{C} \quad (\text{A.2})$$

The surface first Piola-Kirchhoff stress can be derived by Equation (3.6) as follows:

$$\tilde{\mathbf{P}}(\tilde{\mathbf{F}}, \tilde{\mu}) = \frac{\tilde{G}}{\tilde{J}_0} (\tilde{\lambda}_0^2 \tilde{\mathbf{F}} - \tilde{\mathbf{F}}^{-\text{T}}) + \frac{\tilde{\beta}}{\tilde{J}_0} \frac{k_B T}{\tilde{\Omega}} \left[\tilde{J}_0 \ln \left(1 - \frac{1}{\tilde{J}_0 \tilde{J}} \right) + \frac{1}{\tilde{J}} + \frac{\tilde{\chi}}{\tilde{J}_0 \tilde{J}^2} \right] \tilde{\mathbf{F}}^{-\text{T}} - \frac{\tilde{\beta}}{\tilde{J}_0} \frac{\tilde{\mu}}{\tilde{\Omega}} \tilde{\mathbf{F}}^{-\text{T}} \quad (\text{A.3})$$

which corresponds to Equation (3.7b) in manuscript. The initial conditions for hydrogel film at free swollen state are given by:

$$\tilde{J}_0 = \tilde{\lambda}_0^2, \quad \tilde{\mu} = \tilde{\mu}_0, \quad \tilde{\mathbf{F}} = \tilde{\mathbf{I}}, \quad \tilde{J} = 1 \quad (\text{A.4})$$

By substituting Equation (A.4) into Equation (A.3), the surface first Piola-Kirchoff stress at the initial (free swollen) state can be obtained,

$$\frac{1}{G} \tilde{\mathbf{P}}(\tilde{\lambda}_0, \tilde{\mu}_0) = \left(1 - \frac{1}{\tilde{\lambda}_0^2} + \frac{\tilde{\beta}}{N\tilde{\Omega}} \left[\ln \left(1 - \frac{1}{\tilde{\lambda}_0^2} \right) + \frac{1}{\tilde{\lambda}_0^2} + \frac{\tilde{\chi}}{\tilde{\lambda}_0^4} - \frac{\tilde{\mu}_0}{k_B T} \right] \right) \tilde{\mathbf{I}} = \mathbf{0} \quad (\text{A.5})$$

Finally we can obtain the non-linear algebraic equation,

$$1 - \frac{1}{\tilde{\lambda}_0^2} + \frac{\tilde{\beta}}{N\tilde{\Omega}} \left[\ln \left(1 - \frac{1}{\tilde{\lambda}_0^2} \right) + \frac{1}{\tilde{\lambda}_0^2} + \frac{\tilde{\chi}}{\tilde{\lambda}_0^4} - \frac{\tilde{\mu}_0}{k_B T} \right] = 0 \quad (\text{A.6})$$

where the equation determines the initial stretch (free swelling ratio) $\tilde{\lambda}_0$ based on the initial chemical potential $\tilde{\mu}_0$. In this study, we set $\tilde{\mu}_0 = 0$ (fully swollen), $N\tilde{\Omega}/\tilde{\beta} = 10^{-3}$, and $\tilde{\chi} = 0.7705$, resulting in an initial stretch $\tilde{\lambda}_0 \approx 1.42$. With the molecular incompressibility condition in Equation (3.3), we find the initial solvent concentration, as $\tilde{C}_0 \approx 1.0$.

References

- Shaoting Lin, Hyunwoo Yuk, Teng Zhang, German Alberto Parada, Hyunwoo Koo, Cunjiang Yu, and Xuanhe Zhao. Stretchable hydrogel electronics and devices. *Advanced Materials*, 28(22):4497–4505, 2016.
- Jiawei Yang, Ruobing Bai, Baohong Chen, and Zhigang Suo. Hydrogel adhesion: a supramolecular synergy of chemistry, topology, and mechanics. *Advanced Functional Materials*, 30(2):1901693, 2020.
- Brendon M Baker, Britta Trappmann, William Y Wang, Mahmut S Sakar, Iris L Kim, Vivek B Shenoy, Jason A Burdick, and Christopher S Chen. Cell-mediated fibre recruitment drives extracellular matrix mechanosensing in engineered fibrillar microenvironments. *Nature materials*, 14(12):1262–1268, 2015.
- Matthew S Hall, Farid Alisafaei, Ehsan Ban, Xinzeng Feng, Chung-Yuen Hui, Vivek B Shenoy, and Mingming Wu. Fibrous nonlinear elasticity enables positive mechanical feedback between cells and ecms. *Proceedings of the National Academy of Sciences*, 113(49):14043–14048, 2016.
- Jaemin Kim, Erik Mailand, Ida Ang, Mahmut Selman Sakar, and Nikolaos Bouklas. A model for 3d deformation and reconstruction of contractile microtissues. *Soft Matter*, 2020.
- Jaemin Kim, Erik Mailand, Mahmut Selman Sakar, and Nikolaos Bouklas. A model for mechanosensitive cell migration in dynamically morphing soft tissues. *Extreme Mechanics Letters*, 58:101926, 2023a.
- Erik Mailand, Ece Özelçi, Jaemin Kim, Matthias Rüegg, Odysseas Chaliotis, Jon Märki, Nikolaos Bouklas, and Mahmut Selman Sakar. Tissue engineering with mechanically induced solid-fluid transitions. *Advanced Materials*, 34(2):2106149, 2022.
- Tamara Rossy, Tania Distler, Lucas A Meirelles, Joern Pezoldt, Jaemin Kim, Lorenzo Talà, Nikolaos Bouklas, Bart Deplancke, and Alexandre Persat. *Pseudomonas aeruginosa* type iv pili actively induce mucus contraction to form biofilms in tissue-engineered human airways. *PLoS Biology*, 21(8):e3002209, 2023.
- Ramses V Martinez, Ana C Glavan, Christoph Keplinger, Alexis I Oyetibo, and George M Whitesides. Soft actuators and robots that are resistant to mechanical damage. *Advanced Functional Materials*, 24(20):3003–3010, 2014.
- TJ Wallin, James Pikul, and Robert F Shepherd. 3d printing of soft robotic systems. *Nature Reviews Materials*, 3(6):84–100, 2018.
- Lixuan Hu, Pei Lin Chee, Sigit Sugiarto, Yong Yu, Chuanqian Shi, Ren Yan, Zhuoqi Yao, Xuewen Shi, Jiakai Zhi, Dan Kai, et al. Hydrogel-based flexible electronics. *Advanced Materials*, 35(14):2205326, 2023.
- Xie Fu, Hui Tong, Xia Zhang, Kun Zhang, Lyes Douadji, Shuai Kang, Jinling Luo, Ziwei Pan, and Wenqiang Lu. Anisotropic hydrogels with multiscale hierarchy based on ionic conductivity for flexible sensors. *ACS Applied Polymer Materials*, 2023.
- Shing-Yi Cheng, Steven Heilman, Max Wasserman, Shivaun Archer, Michael L Shuler, and Mingming Wu. A hydrogel-based microfluidic device for the studies of directed cell migration. *Lab on a Chip*, 7(6):763–769, 2007.
- Jindrich Kopecek. Hydrogels: From soft contact lenses and implants to self-assembled nanomaterials. *Journal of Polymer Science Part A: Polymer Chemistry*, 47(22):5929–5946, 2009.
- Byung-Wook Park, Jiang Zhuang, Oncay Yasa, and Metin Sitti. Multifunctional bacteria-driven microswimmers for targeted active drug delivery. *ACS nano*, 11(9):8910–8923, 2017.
- Jing Chen, Dong Wang, Long-Hai Wang, Wanjuan Liu, Alan Chiu, Kaavian Shariati, Qingsheng Liu, Xi Wang, Zhe Zhong, James Webb, et al. An adhesive hydrogel with “load-sharing” effect as tissue bandages for drug and cell delivery. *Advanced Materials*, 32(43):2001628, 2020.
- Clinton G Wiener, RA Weiss, and Bryan D Vogt. Overcoming confinement limited swelling in hydrogel thin films using supramolecular interactions. *Soft matter*, 10(35):6705–6712, 2014.
- Jessica Delavoipière, Bertrand Heurtefeu, Jérémie Teisseire, Antoine Chateauminois, Yvette Tran, Marc Fermigier, and Emilie Verneuil. Swelling dynamics of surface-attached hydrogel thin films in vapor flows. *Langmuir*, 34(50):15238–15244, 2018.
- David Moreau, Caroline Chauvet, François Etienne, François P Rannou, and Laurent Corté. Hydrogel films and coatings by swelling-induced gelation. *Proceedings of the National Academy of Sciences*, 113(47):13295–13300, 2016.
- Ni Huo, Sheng Ye, Andrew J Ouderkirk, and Wyatt E Tenhaeff. Porous polymer films with tunable pore size and morphology by vapor deposition. *ACS Applied Polymer Materials*, 4(10):7300–7310, 2022.
- Alessandro Lucantonio, Luciano Teresi, and Antonio DeSimone. Continuum theory of swelling material surfaces with applications to thermo-responsive gel membranes and surface mass transport. *Journal of the Mechanics and Physics of Solids*, 89:96–109, 2016.

- Zhaoqiang Song, Xiaodong Liang, Kai Li, and Shengqiang Cai. Surface mechanics of a stretched elastomer layer bonded on a rigid substrate. *International Journal of Solids and Structures*, 200:1–12, 2020.
- Zhaoqiang Song, Xu Li, Kaijin Wu, and Shengqiang Cai. Nonequilibrium thermodynamic modeling of case ii diffusion in glassy polymers. *Journal of the Mechanics and Physics of Solids*, 179:105395, 2023.
- Chung-Yuen Hui, Fan Cui, Alan Zehnder, and Franck J Vernerey. Physically motivated models of polymer networks with dynamic cross-links: comparative study and future outlook. *Proceedings of the Royal Society A*, 477(2255):20210608, 2021.
- Nikolaos Bouklas and Rui Huang. Swelling kinetics of polymer gels: comparison of linear and nonlinear theories. *Soft Matter*, 8(31):8194–8203, 2012.
- Nikolaos Bouklas, Chad M Landis, and Rui Huang. A nonlinear, transient finite element method for coupled solvent diffusion and large deformation of hydrogels. *Journal of the Mechanics and Physics of Solids*, 79:21–43, 2015.
- Cynthia A Reinhart-King, Micah Dembo, and Daniel A Hammer. The dynamics and mechanics of endothelial cell spreading. *Biophysical journal*, 89(1):676–689, 2005.
- Justin R Tse and Adam J Engler. Preparation of hydrogel substrates with tunable mechanical properties. *Current protocols in cell biology*, 47(1):10–16, 2010.
- Elisabeth G Rens and Roeland MH Merks. Cell shape and durotaxis explained from cell-extracellular matrix forces and focal adhesion dynamics. *Science*, 23(9), 2020.
- Qin Xu, Lawrence A Wilen, Katharine E Jensen, Robert W Style, and Eric R Dufresne. Viscoelastic and poroelastic relaxations of soft solid surfaces. *Physical Review Letters*, 125(23):238002, 2020.
- Martin Björklund, Karl Larsson, and Mats G Larson. Error estimates for finite element approximations of viscoelastic dynamics: The generalized maxwell model. *arXiv preprint arXiv:2311.12667*, 2023.
- Gerhard A Holzapfel. *Nonlinear solid mechanics II*. John Wiley & Sons, Inc., 2000.
- Paul Steinmann. On boundary potential energies in deformational and configurational mechanics. *Journal of the Mechanics and Physics of Solids*, 56(3):772–800, 2008.
- Ali Javili and Paul Steinmann. A finite element framework for continua with boundary energies. part i: the two-dimensional case. *Computer Methods in Applied Mechanics and Engineering*, 198(27-29):2198–2208, 2009.
- A Javili and Paul Steinmann. A finite element framework for continua with boundary energies. part ii: The three-dimensional case. *Computer Methods in Applied Mechanics and Engineering*, 199(9-12):755–765, 2010.
- AT McBride, A Javili, P Steinmann, and Swantje Bargmann. Geometrically nonlinear continuum thermomechanics with surface energies coupled to diffusion. *Journal of the Mechanics and Physics of Solids*, 59(10):2116–2133, 2011.
- Jaemin Kim, Ida Ang, Francesco Ballarin, Chung-Yuen Hui, and Nikolaos Bouklas. A finite element implementation of finite deformation surface and bulk poroelasticity. *Computational Mechanics*, 2023b.
- Wei Hong, Xuanhe Zhao, Jinxiong Zhou, and Zhigang Suo. A theory of coupled diffusion and large deformation in polymeric gels. *Journal of the Mechanics and Physics of Solids*, 56(5):1779–1793, 2008.
- Shawn A Chester and Lallit Anand. A coupled theory of fluid permeation and large deformations for elastomeric materials. *Journal of the Mechanics and Physics of Solids*, 58(11):1879–1906, 2010.
- Alessandro Lucantonio, Paola Nardinocchi, and Luciano Teresi. Transient analysis of swelling-induced large deformations in polymer gels. *Journal of the Mechanics and Physics of Solids*, 61(1):205–218, 2013.
- Shawn A Chester, Claudio V Di Leo, and Lallit Anand. A finite element implementation of a coupled diffusion-deformation theory for elastomeric gels. *International Journal of Solids and Structures*, 52:1–18, 2015.
- Christopher W MacMinn, Eric R Dufresne, and John S Wettlaufer. Large deformations of a soft porous material. *Physical Review Applied*, 5(4):044020, 2016.
- Ivo Babuška. Error-bounds for finite element method. *Numerische Mathematik*, 16(4):322–333, 1971.
- Franco Brezzi. On the existence, uniqueness and approximation of saddle-point problems arising from lagrangian multipliers. *Publications mathématiques et informatique de Rennes*, (S4):1–26, 1974.
- Márcio A Murad and Abimael FD Loula. On stability and convergence of finite element approximations of biot’s consolidation problem. *International Journal for Numerical Methods in Engineering*, 37(4):645–667, 1994.
- Klaus-Jürgen Bathe. The inf-sup condition and its evaluation for mixed finite element methods. *Computers & structures*, 79(2):243–252, 2001.
- P Steinmann, AT McBride, S Bargmann, and A Javili. A deformational and configurational framework for geometrically non-linear continuum thermomechanics coupled to diffusion. *International Journal of Non-Linear Mechanics*, 47(2):215–227, 2012.
- Ida Ang, Zezhou Liu, Jaemin Kim, Chung-Yuen Hui, and Nikolaos Bouklas. Effect of elastocapillarity on the swelling kinetics of hydrogels. *Journal of the Mechanics and Physics of Solids*, page 104132, 2020.
- PJ Flory. Thermodynamic relations for high elastic materials. *Transactions of the Faraday Society*, 57:829–838, 1961.
- Gerhard A Holzapfel, Thomas C Gasser, and Ray W Ogden. A new constitutive framework for arterial wall mechanics and a comparative study of material models. *Journal of elasticity and the physical science of solids*, 61(1-3):1–48, 2000.
- Albert Edward Green and Wolfgang Zerna. *Theoretical elasticity*. Courier Corporation, 1992.
- Manfredo P Do Carmo. *Differential geometry of curves and surfaces: revised and updated second edition*. Courier Dover Publications, 2016.
- Morton E Gurtin, Eliot Fried, and Lallit Anand. *The mechanics and thermodynamics of continua*. Cambridge University Press, 2010.
- Christian Linder, Mykola Tkachuk, and Christian Miehe. A micromechanically motivated diffusion-based transient network model and its incorporation into finite rubber viscoelasticity. *Journal of the Mechanics and Physics of Solids*, 59(10):2134–2156, 2011.
- Paul J Flory and John Rehner Jr. Statistical mechanics of cross-linked polymer networks ii. swelling. *The journal of chemical physics*, 11(11):521–526, 1943.
- Paul J Flory. *Principles of polymer chemistry*. Cornell university press, 1953.
- Fernanda F Fontenele and Nikolaos Bouklas. Understanding the inelastic response of collagen fibrils: A viscoelastic-plastic constitutive model. *Acta Biomaterialia*, 163:78–90, 2023.
- Wei Hong, Zishun Liu, and Zhigang Suo. Inhomogeneous swelling of a gel in equilibrium with a solvent and mechanical load. *International*

- Journal of Solids and Structures*, 46(17):3282–3289, 2009.
- Anders Logg, Kent-Andre Mardal, and Garth N. Wells. *Automated Solution of Differential Equations by the Finite Element Method*. Springer, 2012.
- Martin S. Alnæs, Jan Blechta, Johan Hake, August Johansson, Benjamin Kehlet, Anders Logg, Chris Richardson, Johannes Ring, Marie E. Rognes, and Garth N. Wells. The FEniCS project version 1.5. *Archive of Numerical Software*, 3(100), 2015.
- Thomas JR Hughes. *The finite element method: linear static and dynamic finite element analysis*. Courier Corporation, 2012.
- Cedric Taylor and Paul Hood. A numerical solution of the navier-stokes equations using the finite element technique. *Computers & Fluids*, 1(1): 73–100, 1973.
- Satish Balay, Shrirang Abhyankar, Mark Adams, Jed Brown, Peter Brune, Kris Buschelman, Lisandro Dalcin, Alp Dener, Victor Eijkhout, W Gropp, et al. PETSc users manual. 2019.
- F Ballarin. multiphenics – easy prototyping of multiphysics problems in FEniCS. <https://github.com/multiphenics/multiphenics>, 2019.
- Howard Brenner and LG Leal. A model of surface diffusion on solids. *Journal of Colloid and Interface Science*, 62(2):238–258, 1977.
- Wei H Yang and David J Srolovitz. Surface morphology evolution in stressed solids: surface diffusion controlled crack initiation. *Journal of the Mechanics and Physics of Solids*, 42(10):1551–1574, 1994.
- Christopher M Stafford, Christopher Harrison, Kathryn L Beers, Alamgir Karim, Eric J Amis, Mark R VanLandingham, Ho-Cheol Kim, Willi Volksen, Robert D Miller, and Eva E Simonyi. A buckling-based metrology for measuring the elastic moduli of polymeric thin films. *Nature materials*, 3(8):545–550, 2004.
- Pei-Chun Lin, Shilpi Vajpayee, Anand Jagota, Chung-Yuen Hui, and Shu Yang. Mechanically tunable dry adhesive from wrinkled elastomers. *Soft Matter*, 4(9):1830–1835, 2008.
- Zezhou Liu, Chung-Yuen Hui, Anand Jagota, Jian Ping Gong, and Ryuji Kiyama. A surface flattening method for characterizing the surface stress, drained poisson’s ratio and diffusivity of poroelastic gels. *Soft Matter*, 17(31):7332–7340, 2021.
- Ted Belytschko, Wing Kam Liu, Brian Moran, and Khalil Elkhodary. *Nonlinear finite elements for continua and structures*. John wiley & sons, 2014.
- Jeremy Bleyer. Numerical tours of computational mechanics with fenics. *Zenodo*, 2018.